ACS APPLIED MATERIALS & INTERFACES

www.acsami.org

Research Article

Inorganic Ruddlesden-Popper Faults in Cesium Lead Bromide Perovskite Nanocrystals for Enhanced Optoelectronic Performance

Maria V. Morrell, Alec Pickett, Payal Bhattacharya, Suchismita Guha,* and Yangchuan Xing*

Cite This: *ACS Appl. Mater. Interfaces* 2021, 13, 38579–38585

Read Online

ACCESS | Metrics & More | Article Recommendations | Supporting Information

ABSTRACT: While the layered hybrid Ruddlesden-Popper (RP) halide perovskites have already established themselves as the frontrunners among the candidates in optoelectronics, their all-inorganic counterparts remain least explored in the RP-type perovskite family. Herein, we study and compare the optoelectronic properties of all-inorganic $CsPbBr_3$ perovskite nanocrystals (PNCs) with and without RP planar faults. We find that the RP-$CsPbBr_3$ PNCs possess both higher exciton binding energy and longer exciton lifetimes. The former is ascribed to a quantum confinement effect in the PNCs induced by the RP faults. The latter is attributed to a spatial electron−hole separation across the RP faults. A striking difference is found in the up-conversion photoluminescence response in the two types of $CsPbBr_3$ PNCs. For the first time, all-inorganic RP-$CsPbBr_3$ PNCs are tested in light-emitting devices and shown to significantly outperform the non-RP $CsPbBr_3$ PNCs.

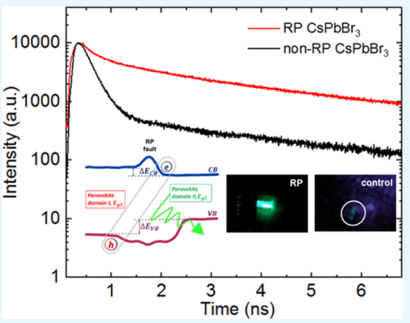

KEYWORDS: *Ruddlesden-Popper fault, exciton binding energy, exciton lifetime, metal-halide perovskites, light emitting diodes*

INTRODUCTION

A family of Ruddlesden-Popper (RP) halide perovskites stands out among other perovskite compounds due to their unique crystalline structure, in which the ABX_3 perovskite layers are interleaved with AX rock-salt type layers, forming an RP phase.[1,2] The RP phase was suggested to contribute to a number of intriguing properties in perovskite oxides, including high T_c superconductivity, colossal magnetoresistance, and ferroelectricity.[3−6] In light of the rapid development in the hybrid halide perovskites in photovoltaics, much attention has been focused on hybrid two-dimensional (2D) or quasi-2D RP or layered perovskites, in which the perovskite slabs, serving as quantum wells, are separated by insulating organic spacers, acting as potential barriers.[7] Within a short period of time, layered 2D halide perovskites have established themselves as excellent candidates for highly efficient and stable solar cells and light-emitting devices (LEDs).[8−12] Owing to their hydrophobic nature, organic spacers effectively shield perovskite layers from moisture—a major stability hurdle in the perovskite-based technology. However, the organic spacers, due to their insulating nature, can induce charge accumulation, impede electron transport, and lead to non-radiative recombination losses.[13] Efforts have been made by reducing the length of organic spacers or implementing all-inorganic RP perovskite nanocrystals (PNCs) with naturally occurring ultrathin RP planar faults.

The existence of the RP phase in all-inorganic $CsPbBr_3$ PNCs was first predicted by Yu et al.[14] Since then, it has been shown that the RP faults in all-inorganic PNCs can be successfully produced via multiple techniques, including stripping passivating ligands with subsequent fusion of PNCs, doping with Mn^{2+}, and mixing halogen anions with a large atomic radius difference (e.g., Cl and I).[15−17] Despite a number of comprehensive reports, the structure−property relationship in all-inorganic RP-PNCs remains inconclusive. This is largely due to the diversity of the inorganic materials serving as hosts of the RP faults. This includes the use of different dopants during synthesis as well as variations in the dimensionality (0D−3D) of the host materials. Along with the lack of control over the formation of RP faults, elucidating the role of such RPs in optoelectronic properties remains a challenge.

Our prior work demonstrated a new chemical route for engineering RP faults in $CsPbBr_3$ PNCs with enhanced photoluminescence properties.[15] This simple post-synthesis treatment has opened up an avenue for the in-depth understanding of the role of RP faults in enhancing the optical properties of $CsPbBr_3$ PNCs. In this work, we determine the exciton binding energy and lifetime of RP-$CsPbBr_3$ PNCs and compare them to the non-RP $CsPbBr_3$ PNCs. For the first time, such all-inorganic RP-$CsPbBr_3$ PNCs were evaluated in LED structures.

Received: April 6, 2021
Accepted: July 26, 2021
Published: August 6, 2021

https://doi.org/10.1021/acsami.1c06350
ACS Appl. Mater. Interfaces 2021, 13, 38579–38585

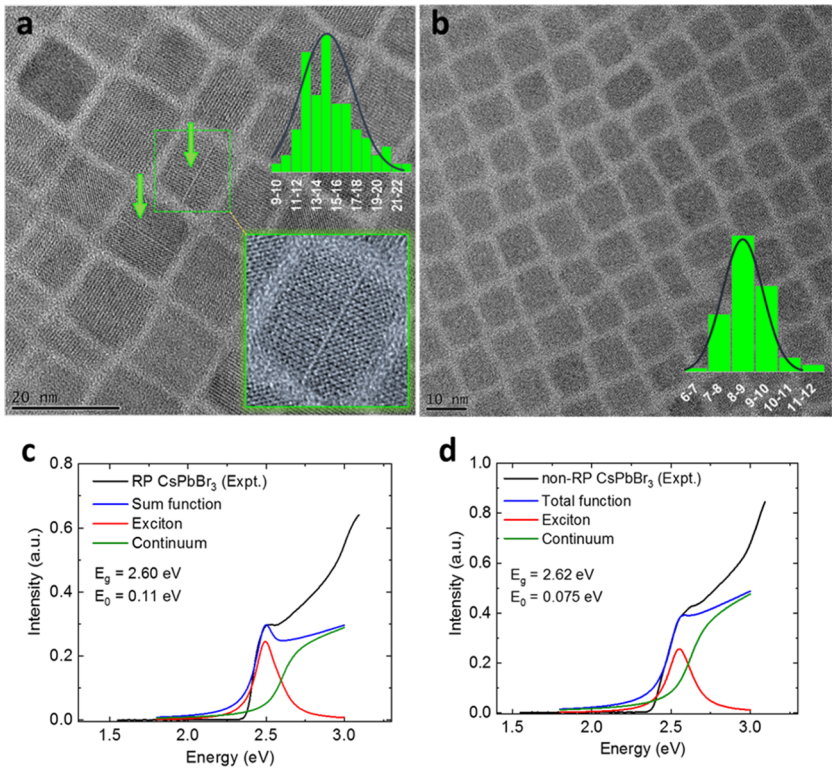

Figure 1. TEM images of RP and non-RP $CsPbBr_3$ PNCs with their size distribution and (c,d) their corresponding UV−vis absorption spectra from colloid samples (experimental and modeled). The bottom inset in (a) shows a close-up image of a RP planar fault.

RESULTS AND DISCUSSION

Exciton Binding Energy. Density functional theory (DFT) calculations of the RP planar faults predicted significant band offsets in both conduction (134 meV) and valence (−193 meV) bands, as well as a higher macroscopic electrostatic potential (~1.5 eV) across the RP boundary.[15,18] Motivated by the theoretical results in the electronic structure changes of the RP-$CsPbBr_3$ PNCs, we estimate the exciton binding energies from the experimentally obtained absorption spectra. The earlier reported red shift for colloid RP-$CsPbBr_3$ PNCs was primarily attributed to a significant growth in the size of the latter.[15] To tackle the size non-homogeneity, the procedure was modified to produce RP-PNCs with a smaller size deviation (*ca.* ~15 nm) from the non-RP $CsPbBr_3$ (*ca.* ~9 nm), as shown in Figure 1a,b from transmission electron microscopy (TEM) images. Yet, the optical response from the colloid PNCs displayed the same characteristic features as before; there is a considerable red shift in the maximum absorption peak but with a rather negligible shift in the absorption onset and a more prominent excitonic peak at room temperature. More than 50 batches of both RP- and non-RP PNCs have been synthesized and analyzed via TEM. The optical spectroscopic measurements were conducted on more than four batches of samples.

The ambient structural properties of RP-$CsPbBr_3$ and non-RP $CsPbBr_3$ are similar and were previously discussed in detail elsewhere.[19] To estimate the binding energies, the absorption data were fitted to the Elliott's model[20]

$$\alpha(\omega) = \alpha_0^{3D}\frac{\hbar\omega}{E_0}\left[\sum_{n=1}^{\infty}\frac{4\pi}{n^3}\delta\left(\Delta + \frac{1}{n^2}\right) + \Theta(\Delta)\frac{\pi e^{-\pi/\sqrt{\Delta}}}{\sinh(\pi/\sqrt{\Delta})}\right] \quad (1)$$

where $\Delta = (\hbar\omega - E_g)/E_0$, E_g is the band gap energy, and E_0 is the exciton binding energy. The first term in the bracket represents the excitonic state and the second term describes the continuum state absorption; n is the principal quantum number and is a step function. A Gaussian line broadening function was used for fitting the experimental absorption spectra.

Interestingly, the exciton binding energy in the colloid RP-$CsPbBr_3$ PNCs was consistently ~35 ± 5 meV higher than that in the non-RP sample, as shown in Figures 1c,d and S1. We also analyzed the absorption spectra from drop-casted thin films of both PNCs. The binding energy in the RP-$CsPbBr_3$ film was found to be ~21 meV larger than that in the non-RP film (see Figure S2). Exciton binding energies are known to increase up to four times with a transition from three-dimensional (3D) to 2D.[21] Further enhancement has been observed in hybrid layered perovskites, where the higher binding energies were attributed to an image charge effect, arising from the difference in dielectric constants between the potential well and the barrier materials.[22,23] In our case, the RP-$CsPbBr_3$ PNCs mainly possess a cuboid shape with a thickness of ~14 nm (exceeding the 2D limit).[15] Therefore, the enhancement in the exciton binding energy is attributed to the RP fault-induced quantum confinement effect, leading to tightly bound excitons.

https://doi.org/10.1021/acsami.1c06350
ACS Appl. Mater. Interfaces 2021, 13, 38579−38585

Exciton Lifetime. To investigate the effect of RP faults on the luminescent properties, we have examined the time-resolved photoluminescence (PL) decay in both types of PNCs. Figure 2 shows typical PL decay curves for the thin

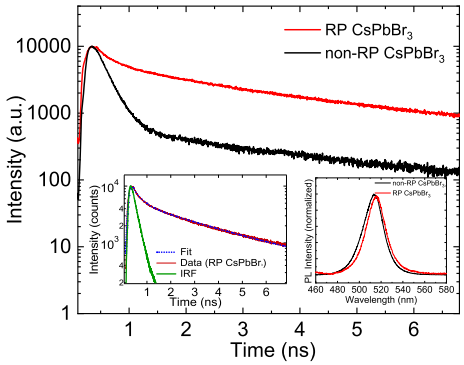

Figure 2. PL relaxation curves for RP and non-RP $CsPbBr_3$ PNCs. The insets show the IRF along with fitted decay data for RP-$CsPbBr_3$ (left) and the normalized PL spectra from the two samples (right).

films of the RP- and non-RP $CsPbBr_3$ PNCs, with their PL spectra shown as insets. As seen, the presence of two relaxation modes, fast and slow, is evident for both PNCs. The corresponding lifetimes and amplitudes were extracted by deconvoluting the instrument response function (IRF) and fitting the PL decay data (see Supporting Information). Remarkably, we observed a substantial difference in the exciton lifetimes. The non-RP $CsPbBr_3$ PNCs were characterized by an average exciton lifetime of ~3.5 ns, whereas the lifetime in RP-$CsPbBr_3$ was found to be more than two times larger at ~7.8 ns.

Longer exciton lifetimes in RP-$CsPbBr_3$ PNCs could potentially arise from a spatial electron−hole separation across the RP faults, similar to that reported for other quantum dots with type II energy band alignment.[24] As such, if the perovskite domains, separated by RP faults, possess different band gaps originating from the difference in grain size, the excited electron would funnel into the domain with a smaller band gap, occupying the lowest available energy level, as illustrated in Figure 3. Given the fine thickness of the RP fault (~3.59 Å) and the observation of electron funneling in layered perovskites with considerably thicker organic spacers,[25] we postulate

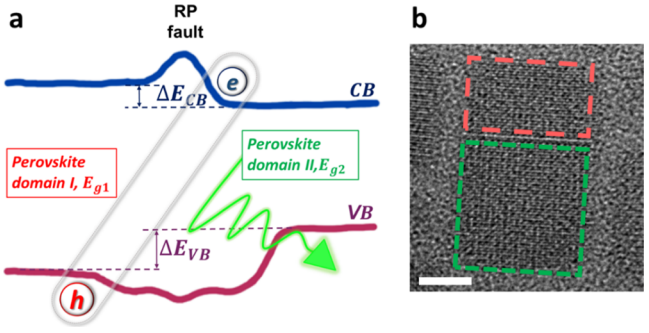

Figure 3. Schematic illustration of spatial electron−hole separation across the RP fault. Both valence and conduction bands were drawn to replicate the shape predicted by the DFT study in ref 18. (b) TEM image of the RP-$CsPbBr_3$ PNC where such phenomenon is suggested to occur. The white bar corresponds to 5 nm.

that the proposed transition is highly probable in RP-$CsPbBr_3$ PNCs.

To verify the size deviation in the perovskite domains separated by the RP faults, we estimated the size of each domain from the collected TEM images. For consistency, larger grains were assigned to domains A and smaller ones, to domains B. The average size of domains A was estimated to be 11 nm, followed by the second most common size of 9 nm. Subsequently, domains B displayed the average size of 4 nm, followed by 6 and 8 nm (Figure S4). Lin et al. demonstrated that the band gap structure of $CsPbBr_3$ PNCs was governed by the shortest dimension (rather than volume) and could be altered with the change as small as 1 nm. The ~3 nm reduction in the edge length resulted in an increase of the band gap by 16 meV and 12 meV for isolated PNCs and their ensemble, respectively.[26] When we compared domains A to their corresponding domains B for each RP-PNC, we found that the most frequent deviations in size were 4 and 5 nm (Figure S4). This lends further support to the suggested spatial electron−hole separation across the RP fault driven by the difference in the band alignment of the adjacent domains.

The percentage contribution and lifetimes for each of the components are summarized in Table 1. The PL emission in

Table 1. Percentage Contribution and Lifetimes Corresponding to Short and Long Relaxation Modes for RP and Non-RP $CsPbBr_3$ PNCs[a]

	long component		short component	
	A [%]	τ_1 [ns]	B [%]	τ_2 [ns]
non-RP	33	3.24 ± 0.28	67	0.24 ± 0.01
RP	83	3.07 ± 0.07	17	0.30 ± 0.02

[a]A and B are the fitting constants in the PL decay functions (see SI).

the non-RP-$CsPbBr_3$ thin films was mainly driven by the exciton (band-edge) recombination (~67%). Whereas in the RP-$CsPbBr_3$ thin films, the contribution from a short component dropped down to ~17%, and the PL emission was primarily determined by the long relaxation mode generally associated with trapped luminescence.[27]

It is evident that the formation of RP faults in $CsPbBr_3$ PNCs has a major impact on the nature of the PL emission. Trapped luminescence in semiconductor quantum dots is believed to arise from sub-gap trap states or surface states.[28] It has been widely accepted that $CsPbBr_3$ PNCs possess high defect tolerance, meaning that most point defects are shallow and do not introduce deep-level states capable of trapping charge carriers.[29] Furthermore, the DFT-based calculations of all plausible point defects at the RP boundaries did not predict any sub-gap states, except Pb dangling bonds, similar to non-RP PNCs.[18] In addition, TEM image analysis of the experimentally developed RP faults did not reveal any defects in the CsBr layers.[18] However, multi-exponential PL decay combined with the existence of up-conversion PL (UC-PL) in all-inorganic PNCs suggests the existence of intermediate sub-gap states.[30−32]

Given the specific approach used for the formation of RP faults in our $CsPbBr_3$ PNCs, in particular the stripping of stabilizing ligands from the surface of $CsPbBr_3$, we believe that the trapped luminescence is realized via surface states, which are exposed due to a reduced density of passivating ligands on the RP-$CsPbBr_3$ PNCs. The latter is apparent as continuous growth with time of the RP-$CsPbBr_3$ PNCs in their colloids

https://doi.org/10.1021/acsami.1c06350
ACS Appl. Mater. Interfaces 2021, 13, 38579−38585

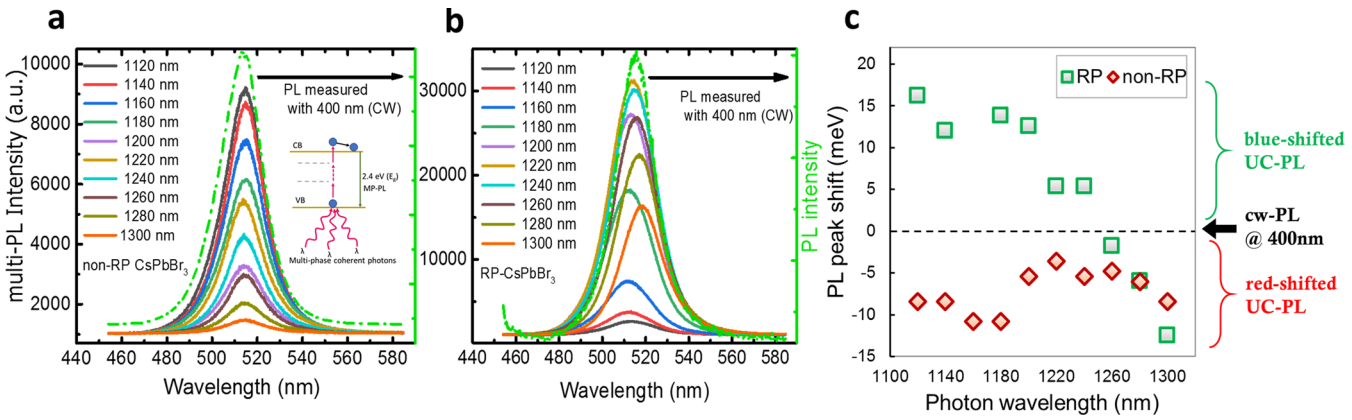

Figure 4. Up-conversion photoluminescence spectra from (a) non-RP $CsPbBr_3$ and (b) RP- $CsPbBr_3$ PNCs with their corresponding cw-PL (green dashed). (c) Comparative analysis of the UC-PL peak position shift with respect to the cw-PL peak. The inset in (a) illustrates the mechanism of multiphoton absorption.

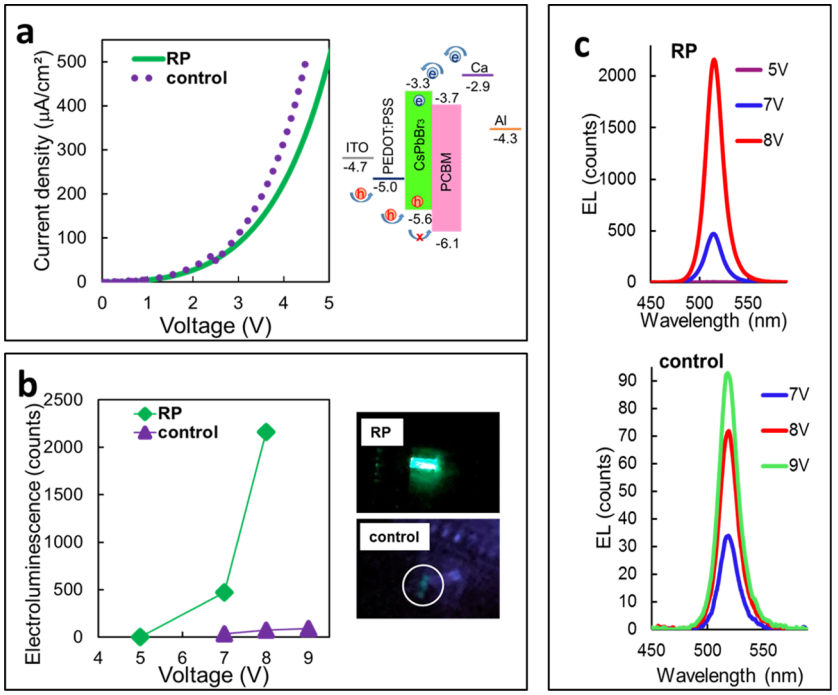

Figure 5. Current density−voltage characteristics of the RP and control LEDs with the energy (in eV) diagram corresponding to the ITO/PEDOT:PSS/Perovskite/PCBM/Ca/Al architecture. (b) Comparative analysis of the electroluminescence (EL) from RP and control LEDs with corresponding images of the devices taken in the dark under the same voltage applied. (c) EL spectra matching the data points in (b) for RP (top) and control (bottom) LEDs.

was observed. Additionally, the growth is accompanied by the formation of an extensive network of RP faults (see Figure S3). The sub-gap surface states may serve as a reservoir for the excited states. However, despite that surface states are involved in light emission, the removal of the passivating ligands does not reduce the overall PL quantum yield.[15] Consequently, the RP faults allow an efficient process for re- and de-population of the sub-gap states in the RP PNCs.

Multi-Photon UC-PL. Halide perovskites show strong nonlinear optical properties including multiphoton absorption and emission, which further yield insights into sub-gap states.[33] We have measured the UC-PL in both types of $CsPbBr_3$ PNCs. Thin films were drop-casted onto glass substrates and excited with pulsed laser excitation below the energy band gap, in the range of 1120−1300 nm, as shown in Figure 4a,b. The spectra were then compared to the continuous wave PL (cw-PL), collected with a 400 nm excitation source, to estimate the shift in the maximum PL peak position.

A striking difference was discovered in the UC-PL response from both RP and non-RP $CsPbBr_3$ films, which is presented in Figure 4c. The data acquired from the non-RP $CsPbBr_3$ is in good agreement with the previous results of UC-PL in $CsPbBr_3$ PNCs.[31,32] Specifically, the UC-PL from the PNCs displayed a characteristic red shift with respect to the cw-PL. Whereas, the UC-PL in RP-$CsPbBr_3$ PNCs was characterized by a red shift in the range of 1300−1260 nm, with an apparent blue shift starting at ∼1240 nm. Furthermore, the UC-PL intensity in the 1300−1260 nm excitation range, measured under the same conditions, was significantly stronger in the RP-PNCs than in the non-RP PNCs.

https://doi.org/10.1021/acsami.1c06350
ACS Appl. Mater. Interfaces 2021, 13, 38579−38585

Intriguingly, around the transition point to higher emission energies, the UC-PL intensities in the RP-film start decreasing. We speculate that the red shift in UC-PL spectra in both types of PNCs stems from a recombination of excited carriers from the surface states, located below the conduction band, to the valence band (see Figure S5). Assuming that the RP-PNCs possess a higher density of such states due to the aforementioned loss of stabilizing ligands, the higher binding energies in RP films prevent the excitons from dissociation and therefore result in stronger UC-PL. It is likely that the blue shift occurs when the excited electrons recombine from the states above the conduction minimum band.[34] However, since the blue shift in UC-PL spectra is specific to RP-films only, it would be reasonable to attribute it to the presence of RPs, precisely to the expansion of the band gap due to the band offset across the RP boundary by ∼327 meV.[18] The origin of the red and blue shifts seen in the UC-PL is schematically illustrated in Figure S5. The obtained data explicitly shows a substantial impact of the RPs on the optoelectronic properties of the $CsPbBr_3$ PNCs.

Application in LEDs. Both the enhanced binding energies and longer exciton lifetimes are strongly desired for highly efficient LEDs. Driven by these observations and our prior report of the enhanced PL stability in RP-$CsPbBr_3$, we fabricated LEDs with both types of PNCs using the following architecture: ITO/PEDOT:PSS/Perovskite/PCBM/Ca/Al. To our knowledge, this is the first demonstration of all-inorganic $CsPbBr_3$ containing RP faults in LEDs. More than 12 substrates with 6 LEDs on each were prepared for both RP- and non-RP PNCs. PCBM is a common choice for the n-type layer in thin-film LEDs and primarily works as an electron-transporting layer (ETL). However, the PCBM in our case serves as a hole-blocking layer (rather than the ETL), as shown in Figure 5a. Al was deposited on top of the Ca to prevent oxidation. For simplicity, LEDs assembled using the RP and non-RP $CsPbBr_3$ PNC are referred to as "RP" and "control", respectively.

A comparative analysis of the RP and control LEDs showed that both devices displayed relatively similar current-density characteristics in the range from 0 to 5 V with about the same turn-on voltages (Figure 5a). As expected, both devices demonstrated stronger EL when higher voltages were applied. However, the RP LEDs exhibited a significantly stronger EL under the same conditions (Figure 5b). The experimental setup for the control and RP LEDs was identical; hence, we can directly compare the EL intensities from the two samples. Additionally, similar to organic layered perovskites, the RP-LEDs demonstrated a higher lifespan under ambient conditions. Several devices were fabricated without the PCBM layer and their EL was monitored over a few days (Figure S6). Considerably low performance in the control devices could be due to a poor morphology of the non-RP film. Given the smaller size of non-RP $CsPbBr_3$ PNCs, it is quite challenging to produce a pinhole-free thin film. Pinholes in the emissive layer could lead to significant current losses and, as such, result in lower efficiencies of the device. However, the analysis of the film morphologies using electron micrographs eliminated this reasoning. Both films were found to be reasonably similar in terms of packing density or film porosity (see Figures S7−S10 in Supporting Information). The higher EL in the RP-LEDs is therefore a ramification of the presence of the RP faults that lead to higher exciton binding energy and longer lifetimes.

CONCLUSIONS

In summary, our findings suggest that the formation of RP planar faults in $CsPbBr_3$ PNCs affects their optoelectronic properties substantially. Specifically, we found that the RP-$CsPbBr_3$ PNCs possessed higher exciton binding energy and exhibited longer exciton lifetimes. The increase in binding energies was attributed to the RP-induced quantum confinement of excitons within the perovskite grains, cleaved by the insulating CsBr bi-layers. Longer exciton lifetimes were ascribed to the spatial electron−hole separation and were suggested to originate from the surface states. The latter appear due to the removal of the stabilizing ligands and serve as a reservoir for the excited states, while the RP faults allow their efficient repopulation. RP-$CsPbBr_3$ PNCs were also shown to outperform non-RP PNCs in LEDs. These findings suggest that engineering the RP faults in $CsPbBr_3$ PNCs can serve as an excellent pathway toward improving perovskite-based optoelectronics.

EXPERIMENTAL SECTION

Synthesis of $CsPbBr_3$ PNCs. $CsPbBr_3$ PNCs were synthesized by the hot-injection method first reported by Kovalenko's group.[35] Cs_2CO_3 (0.407 g, Aldrich, 99%) was loaded into a 50 mL 3-neck flask along with octadecene (ODE, 20 mL, Aldrich, 90%) and oleic acid (OA, 1.25 mL, Sigma-Aldrich, 90%), dried up in a vacuum for 1 h at 120 °C, and then heated up to 150 °C under a N_2 atmosphere until all Cs_2CO_3 had reacted with OA. $PbBr_2$ (0.069 g, Aldrich, 99.999%) was loaded into a 25 mL 3-neck flask along with ODE (5 mL) and dried up in a vacuum for 1 h at 120 °C. OA (0.5 mL) and oleylamine (OLA, 0.5 mL, Aldrich, 70%) were then injected at 120 °C under a N_2 atmosphere. After complete solubilization of $PbBr_2$, the temperature was raised to 180 °C and Cs-oleate (0.4 mL), preheated to 100 °C, was injected. At ∼10 s, the PNCs were cooled down with a water-ice bath. The PNCs were then centrifuged at 4000 rpm for 12 min. After the supernatant was decanted, the PNCs were redispersed in *n*-heptane (anhydrous, Sigma-Aldrich, 99%). Hereafter, the product is referred to as non-RP $CsPbBr_3$ PNCs.

Formation of RP Faults in $CsPbBr_3$ PNCs. Prior to centrifugation at 4000 rpm for 12 min, ethyl acetate (8 mL, Sigma-Aldrich, ≥99.5%) was added to the PNCs solution (in ODE) to help remove the excess of organic compounds. The supernatant was decanted, and the PNCs were redispersed in *n*-heptane (1 mL). The PNCs were then transferred into the glovebox where 0.2 M diethylzinc (DEZ, Aldrich, ≥52 wt % Zn basis) in *n*-heptane anhydrous was injected at room temperature under an Ar atmosphere. Hereafter, the product is referred to as RP-$CsPbBr_3$ PNCs. Injection of DEZ into PNC solutions with higher concentrations (compared to the original report[15]) was found to significantly narrow the size distribution of the resulting RP-$CsPbBr_3$ and produce a higher occurrence of RPs in PNCs.

$CsPbBr_3$-Based Thin-Film LED Fabrication. Pre-patterned indium tin oxide (ITO) substrates (Ossila, 20 Ω/square) were cleaned using ultrasonication in acetone and isopropanol for 10 min, respectively, rinsed with deionized water, and dried with N_2. ITO substrates were then treated with oxygen plasma for 10 min. Poly(3,4-ethylenedioxythiophene) polystyrene sulfonate (PEDOT:PSS, CLEVIOS P VP AI 4083) solution was deposited using a spin-coater at 5000 rpm for 60 s and annealed at 140 °C for 15 min under N_2. Subsequently, a perovskite layer was deposited at 2000 rpm for 60 s and annealed in the air at 70 °C for 30 min [6,6]-Phenyl-C61-butyric acid methyl ester ([C60]PCBM, nano-c) was dissolved in chloroform and 1,4-dichlorobenzene in 1:1 ratio and deposited on top of the perovskite at 900 rpm for 60 s, followed by annealing in the air for 5 min at 115 °C. Ca and Al were deposited sequentially using thermal evaporation. All devices were encapsulated under N_2 with light-curable epoxy.

https://doi.org/10.1021/acsami.1c06350
ACS Appl. Mater. Interfaces 2021, 13, 38579−38585

Characterization Methods. TEM images were obtained with FEI Tecnai F30 Twin 300 kV transmission electron microscope. UV−vis absorption and PL spectra from $CsPbBr_3$ thin films, drop-casted on glass substrates, were collected with Ocean Optics USB 2000 spectrometer. UV−vis absorption spectra from colloid samples were collected with an Agilent Cary 60 UV−vis spectrophotometer. UC-PL from drop-casted thin films was obtained with an iHR320 f/4.1 spectrometer and a charge-coupled device camera from JYHORIBA in reflection geometry. The excitation wavelength of 1120−1300 nm was obtained from an optical parametric amplifier (TOPAS) using a regenerative amplifier (Spitfire Ace, Spectra Physics) with a repetition rate of 1 kHz, pulse duration of 100 fs, and seeded by a Ti:Sapphire laser (Mai Tai, Spectra Physics). Film Morphology and energy-dispersive X-ray (EDX) spectroscopy were performed with an FEI Quanta 600 FEG Environmental Scanning Electron Microscope. Current Density−Voltage ($J-V$) characteristics of the LEDs were measured using a Keithley 2400 source-meter unit. EL response from LEDs was collected using Ocean Optics USB 2000 spectrometer. Time-resolved photoluminescence (TR-PL) measurements were performed using a time-correlated single-photon counting (TCSPC) technique. The PL lifetimes were measured with a PicoHarp 300 TCSPC module with 4 ps time resolution. The excitation wavelength of 400 nm was generated by frequency doubling the 800 nm wavelength (100 fs, 80 MHz) from a Ti-Sapphire laser (Mai Tai, Spectra Physics). The PL emission from the sample was collected by an avalanche photon counting detector module (Micro Photon Devices), using a long-pass 400 nm filter to eliminate the excitation wavelength.

■ ASSOCIATED CONTENT

Supporting Information

The Supporting Information is available free of charge at https://pubs.acs.org/doi/10.1021/acsami.1c06350.

Time-resolved photoluminescence; UV-vis absorption spectra from colloid samples from different batches for RP and non-RP samples; UV-vis absorption spectra for RP and non-RP $CsPbBr_3$ thin films; HR TEM image of a grown in time RP-$CsPbBr_3$ PNC; TEM images of RP-$CsPbBr_3$ PNCs; illustration of the UC-PL process corresponding to the blue and red shifts; electroluminescence intensity of the ETL-free LEDs with and without RPs; SEM images of perovskite films in control and RP LEDs with corresponding porosity analysis; and EDX spectra obtained from the RP-film with and without agglomerates of interest (PDF)

■ AUTHOR INFORMATION

Corresponding Authors

Suchismita Guha − *Department of Physics and Astronomy, University of Missouri, Columbia, Missouri 65211, United States;* orcid.org/0000-0002-6269-2298; Email: guhas@missouri.edu

Yangchuan Xing − *Department of Biomedical, Biological & Chemical Engineering, University of Missouri, Columbia, Missouri 65211, United States;* orcid.org/0000-0002-5985-3222; Email: xingy@missouri.edu

Authors

Maria V. Morrell − *Department of Biomedical, Biological & Chemical Engineering, University of Missouri, Columbia, Missouri 65211, United States*

Alec Pickett − *Department of Physics and Astronomy, University of Missouri, Columbia, Missouri 65211, United States*

Payal Bhattacharya − *Department of Physics and Astronomy, University of Missouri, Columbia, Missouri 65211, United States*

Complete contact information is available at: https://pubs.acs.org/10.1021/acsami.1c06350

Notes

The authors declare no competing financial interest.

■ ACKNOWLEDGMENTS

S.G. acknowledges partial support of this work through the National Science Foundation under grant nos. DMR-1807263 and ECCS-1827846. Partial support from an incentive funding from the College of Engineering and Electron Microscopy Core at the University of Missouri is acknowledged. We would like to thank David Stalla from the University of Missouri Electron Microscopy Center for SEM and EDX study of the perovskite films, and Carsten A. Ullrich for his help with theoretical programing of the excitonic properties.

■ REFERENCES

(1) Ruddlesden, S. N.; Popper, P. New Compounds of the K_2NiF_4 Type. *Acta Crystallogr.* **1957**, *10*, 538−539.

(2) Ruddlesden, S. N.; Popper, P. The Compound $Sr_3Ti_2O_7$ and Its Structure. *Acta Crystallogr.* **1958**, *11*, 54−55.

(3) Dwiwedi, A.; Cormack, A. N. Crystal Chemistry of Ruddlesden-Popper Type Structures in High *Tc* Ceramic Superconductors. *Bull. Mater. Sci.* **1991**, *14*, 575−584.

(4) Battle, P. D.; Blundell, S. J.; Green, M. A.; Hayes, W.; Honold, M.; Klehe, A. K.; Laskey, N. S.; Millburn, J. E.; Murphy, L.; Rosseinsky, M. J.; Samarin, N. A.; Singleton, J.; Sluchanko, N. E.; Sullivan, S. P.; Vente, J. F. Colossal Magnetoresistance in $Sr_{2-x}Nd_{1+x}Mn_2O_7$ (x=0.0, 0.1). *J. Phys.: Condens. Matter* **1996**, *8*, L427−L434.

(5) Birol, T.; Benedek, N. A.; Fennie, C. J. Interface Control of Emergent Ferroic Order in Ruddlesden-Popper $Sr_{n+1}Ti_nO_{3n+1}$. *J. Phys. Rev. Lett.* **2011**, *107*, 257602.

(6) Oh, Y. S.; Luo, X.; Huang, F.-T.; Wang, Y.; Cheong, S.-W. Experimental Demonstration of Hybrid Improper Ferroelectricity and the Presence of Abundant Charged Walls in $(Ca,Sr)_3Ti_2O_7$ Crystals. *Nat. Mater.* **2015**, *14*, 407−413.

(7) Chen, Z.; Guo, Y.; Wertz, E.; Shi, J. Merits and Challenges of Ruddlesden-Popper Soft Halide Perovskites on Electro-Optics and Optoelectronics. *Adv. Mater.* **2018**, *31*, 1803514.

(8) Tsai, H.; Nie, W.; Blancon, J.-C.; Stoumpos, C. C.; Asadpour, R.; Harutyunyan, B.; Neukirch, A. J.; Verduzco, R.; Crochet, J. J.; Tretiak, S.; Pedesseau, L.; Even, J.; Alam, M. A.; Gupta, G.; Lou, J.; Ajayan, P. M.; Bedzyk, M. J.; Kanatzidis, M. G.; Mohite, A. D. High-Efficiency Two-Dimensional Ruddlesden-Popper Perovskite Solar Cells. *Nature* **2016**, *536*, 312−316.

(9) Cao, D. H.; Stoumpos, C. C.; Farha, O. K.; Hupp, J. T.; Kanatzidis, M. G. 2D Homologous Perovskites as Light-Absorbing Materials for Solar Cell Applications. *J. Am. Chem. Soc.* **2015**, *137*, 7843−7850.

(10) Tsai, H.; Nie, W.; Blancon, J. C.; Stoumpos, C. C.; Soe, C. M. M.; Yoo, J.; Crochet, J.; Tretiak, S.; Even, J.; Sadhanala, A.; Azzellino, G.; Brenes, R.; Ajayan, P. M.; Bulović, V.; Stranks, S. D.; Friend, R. H.; Kanatzidis, M. G.; Mohite, A. D. Stable Light-Emitting Diodes Using Phase-Pure Ruddlesden-Popper Layered Perovskites. *Adv. Mater.* **2018**, *30*, 1704217.

(11) Yang, X.; Zhang, X.; Deng, J.; Chu, Z.; Jiang, Q.; Meng, J.; Wang, P.; Zhang, L.; Yin, Z.; You, J. Efficient Green Light-Emitting Diodes Based on Quasi-Two-Dimensional Composition and Phase Engineered Perovskite with Surface Passivation. *Nat. Commun.* **2018**, *9*, 570.

(12) Wang, N.; Cheng, L.; Ge, R.; Zhang, S.; Miao, Y.; Zou, W.; Yi, C.; Sun, Y.; Cao, Y.; Yang, R.; Wei, Y.; Guo, Q.; Ke, Y.; Yu, M.; Jin, Y.; Liu, Y.; Ding, Q.; Di, D.; Yang, L.; Xing, G.; Tian, H.; Jin, C.; Gao, F.; Friend, R. H.; Wang, J.; Huang, W. Perovskite Light-Emitting Diodes Based on Solution-Processed Self-Organized Multiple Quantum Wells. *Nat. Photonics* **2016**, *10*, 699−704.
(13) Chen, Y.; Sun, Y.; Peng, J.; Tang, J.; Zheng, K.; Liang, Z. 2D Ruddlesden-Popper Perovskites for Optoelectronics. *Adv. Mater.* **2017**, *30*, 1703487.
(14) Yu, Y.; Zhang, D.; Yang, P. Ruddlesden-Popper Phase in Two-Dimensional Inorganic Halide Perovskites: A Plausible Model and Supporting Observations. *Nano Lett.* **2017**, *17*, 5489−5494.
(15) Morrell, M. V.; He, X.; Luo, G.; Thind, A. S.; White, T. A.; Hachtel, J. A.; Borisevich, A. Y.; Idrobo, J.-C.; Mishra, R.; Xing, Y. Significantly Enhanced Emission Stability of CsPbBr3 Nanocrystals via Chemically Induced Fusion Growth for Optoelectronic Devices. *ACS Appl. Nano Mater.* **2018**, *1*, 6091−6098.
(16) Paul, S.; Bladt, E.; Richter, A. F.; Döblinger, M.; Tong, Y.; Huang, H.; Dey, A.; Bals, S.; Debnath, T.; Polavarapu, L.; Feldmann, J. Manganese-Doping-Induced Quantum Confinement within Host Perovskite Nanocrystals through Ruddlesden-Popper Defects. *Angew. Chem., Int. Ed.* **2020**, *59*, 6794−6799.
(17) Akkerman, Q. A.; Bladt, E.; Petralanda, U.; Dang, Z.; Sartori, E.; Baranov, D.; Abdelhady, A. L.; Infante, I.; Bals, S.; Manna, L. Fully Inorganic Ruddlesden−Popper Double Cl−I and Triple Cl−Br−I Lead Halide Perovskite Nanocrystals. *Chem. Mater.* **2019**, *31*, 2182−2190.
(18) Thind, A. S.; Luo, G.; Hachtel, J. A.; Morrell, M. V.; Cho, S. B.; Borisevich, A. Y.; Idrobo, J. C.; Xing, Y.; Mishra, R. Atomic Structure and Electrical Activity of Grain Boundaries and Ruddlesden−Popper Faults in Cesium Lead Bromide Perovskite. *Adv. Mater.* **2019**, *31*, 1805047.
(19) Yesudhas, S.; Morrell, M. V.; Anderson, M. J.; Ullrich, C. A.; Kenney-Benson, C.; Xing, Y.; Guha, S. Pressure-Induced Phase Changes in Cesium Lead Bromide Perovskite Nanocrystals with and without Ruddlesden−Popper Faults. *Chem. Mater.* **2020**, *32*, 785−794.
(20) Haug, H.; Koch, S. W. *Quantum Theory of the Optical and Electronic Properties of Semiconductors*; World Scientific, 2004.
(21) Shinada, M.; Sugano, S. Interband Optical Transitions in Extremely Anisotropic Semiconductors. Bound and Unbound Exciton Absorption. *J. Phys. Soc. Jpn.* **1966**, *21*, 1936−1946.
(22) Ishihara, T. Optical Properties of PbI-based Perovskite Structures. *J. Lumin.* **1994**, *60*−*61*, 269−274.
(23) Tanaka, K.; Takahashi, T.; Kondo, T.; Umebayashi, T.; Asai, K.; Ema, K. Image Charge Effect on Two-Dimensional Excitons in an Inorganic-Organic Quantum-Well Crystal. *Phys. Rev. B: Condens. Matter Mater. Phys.* **2005**, *71*, 045312.
(24) Xu, F.; Volkov, V.; Zhu, Y.; Bai, H.; Rea, A.; Valappil, N. V.; Su, W.; Gao, X.; Kuskovsky, I. L.; Matsui, H. Long Electron-Hole Separation of ZnO-CdS Core-Shell Quantum Dots. *J. Phys. Chem. C* **2009**, *113*, 19419−19423.
(25) Yuan, M.; Quan, L. N.; Comin, R.; Walters, G.; Sabatini, R.; Voznyy, O.; Hoogland, S.; Zhao, Y.; Beauregard, E. M.; Kanjanaboos, P.; Lu, Z.; Kim, D. H.; Sargent, E. H. Perovskite Energy Funnels For Efficient Light-Emitting Diodes. *Nat. Nanotechnol.* **2016**, *11*, 872−877.
(26) Lin, J.; Gomez, L.; de Weerd, C.; Fujiwara, Y.; Gregorkiewicz, T.; Suenaga, K. Direct Observation of Band Structure Modifications in Nanocrystals of $CsPbBr_3$ Perovskite. *Nano Lett.* **2016**, *16*, 7198−7202.
(27) Wu, W.; Gao, Y.; Chang, Q.; Ye, H.; Zheng, Z.; Liu, W.; Li, A.; Yang, Y. Upconversion Luminescent Characteristics and Peak Shift of CdSeS Nanocrystals under Different Wavelength Laser Excitation. *J. Nanopart. Res.* **2011**, *13*, 1049−1061.
(28) Peterson, M. D.; Cass, L. C.; Harris, R. D.; Edme, K.; Sung, K.; Weiss, E. A. The Role of Ligands in Determining the Exciton Relaxation Dynamics in Semiconductor Quantum Dots. *Annu. Rev. Phys. Chem.* **2014**, *65*, 317−339.
(29) Kang, J.; Wang, L.-W. High Defect Tolerance in Lead Halide Perovskite $CsPbBr_3$. *J. Phys. Chem. Lett.* **2017**, *8*, 489−493.
(30) Koscher, B. A.; Swabeck, J. K.; Bronstein, N. D.; Alivisatos, A. P. Essentially Trap-Free $CsPbBr_3$ Colloidal Nanocrystals by Postsynthetic Thiocyanate Surface Treatment. *J. Am. Chem. Soc.* **2017**, *139*, 6566−6569.
(31) Ye, S.; Zhao, M.; Yu, M.; Zhu, M.; Yan, W.; Song, J.; Qu, J. Mechanistic Investigation of Upconversion Photoluminescence in All-Inorganic Perovskite $CsPbBrI_2$ Nanocrystals. *J. Phys. Chem. C* **2018**, *122*, 3152−3156.
(32) Wang, Y.; Li, X.; Zhao, X.; Xiao, L.; Zeng, H.; Sun, H. Nonlinear Absorption and Low-Threshold Pumped Stimulated Emission from All-Inorganic Perovskite Nanocrystals. *Nano Lett.* **2016**, *16*, 448−453.
(33) Morrow, D. J.; Hautzinger, M. P.; Lafayette, D. P.; Scheeler, J. M.; Dang, L.; Leng, M.; Kohler, D. D.; Wheaton, A. M.; Fu, Y.; Guzei, I. A.; Tang, J.; Jin, S.; Wright, J. C. Disentangling second harmonic generation from multiphoton photoluminescence in halide perovskites using multidimensional harmonic generation. *J. Phys. Chem. Lett.* **2020**, *11*, 6551−6559.
(34) Mandal, S.; Mukherjee, S.; De, C. K.; Roy, D.; Ghosh, S.; Mandal, P. K. Extent of Shallow/Deep Trap States beyond the Conduction Band Minimum in Defect-Tolerant $CsPbBr_3$ Perovskite Quantum Dot: Control over the Degree of Charge Carrier Recombination. *J. Phys. Chem. Lett.* **2020**, *11*, 1702−1707.
(35) Protesescu, L.; Yakunin, S.; Bodnarchuk, M. I.; Krieg, F.; Caputo, R.; Hendon, C. H.; Yang, R.; Walsh, A.; Kovalenko, M. V. Nanocrystals of Cesium Lead Halide Perovskites ($CsPbX_3$, X = Cl, Br, and I): Novel Optoelectronic Materials Showing Bright Emission with Wide Color Gamut. *Nano Lett.* **2015**, *6*, 3692−3696.

https://doi.org/10.1021/acsami.1c06350
ACS Appl. Mater. Interfaces 2021, 13, 38579−38585